*Int. J. Electrochem. Sci.*, 11 **(2016)** 23 - 33

International Journal of
ELECTROCHEMICAL
SCIENCE
www.electrochemsci.org

# Three-Dimensional (3D) Nanocomposites of $MnO_2$-Modified Mesoporous Carbon Filled with Carbon Spheres/Carbon Blacks for Supercapacitors

*Zhong Quan Wen*[1,*], *Min Li*[1], *Shi Jin Zhu*[2], *Tian Wang*[2]

[1]College of Optoelectronic Engineering, Key Laboratory of Fundamental Science of Micro/Nano-Devices and System Technology, Chongqing University, Chongqing 400044, PR China
[2]College of Materials Science and Engineering, Chongqing University, Chongqing 400044, PR China
[*]E-mail: wenzq66@163.com

*Received:* 25 October 2015 / *Accepted:* 19 November 2015 / *Published:* 1 December 2015

Herein, three-dimensional (3D) nanocomposites of diverse carbon materials, (e.g., mesoporous carbon (MC) filled with carbon spheres (CS) and carbon blacks (CB)) and $MnO_2$ were synthesized and explored for high-performance supercapacitors. By tuning the amount of $KMnO_4$ the morphology and pore structure of MC-CS-$MnO_2$ and MC-CB-$MnO_2$ nanocomposites could be controlled. A series of electrochemical measurements were performed, exhibiting higher specific capacitance and stable cycling performance of the 3D nanocomposites. Meanwhile, MC-CS-$MnO_2$ demonstrated the larger specific capacitance of 326 F $g^{-1}$ and interestingly an increase specific capacitance for MC-CB-$MnO_2$ was found after 1000 cycles. In principle, these findings show great potential in developing long cycling and electrochemically stable supercapacitors.

**Keywords:** mesoporous carbon; carbon spheres; carbon blacks; manganese dioxide; supercapacitors

## 1. INTRODUCTION

In the last few years, supercapacitors have drawn great attention as they possess a higher power density, excellent cycling stability, rapid charge/discharge course and broad operating temperature range[1-4,11]. On the basis of energy storage mechanism, supercapacitors are normally distributed into electrochemical double layer capacitors (EDLC) and pseudocapacitors. For EDLC, it is crucial that electrode materials own good electrical conductivity and chemical stability, in addition to the high surface area and controlled pore configuration. Besides, pseudocapacitance originating from some transition metal oxides or hydroxides has been studied as well [5-7].

Recently, manganese dioxide ($MnO_2$) has been widely acknowledged as an electrode material for supercapacitors as they possess some attractive performance such as the high theoretical specific capacitance (1370 F $g^{-1}$), environmental friendliness and so on [8,9,20]. However, the emersion of capacity was surely impeded by the poor electrical conductivity of manganese dioxide electrodes which leads to a poor rate capability [10,22]. In fact, the electrochemical capacitance of $MnO_2$ can be observably enhanced by combining $MnO_2$ with carbon nanomaterials [12]. Nowadays, advancements in carbon nanomaterials, such as mesoporous carbon, carbon spheres and graphene, all of which reveal large surface areas, high electrical conductivities, and good chemical stabilities, are leading to considerable interest in using these nanomaterials for supercapacitor applications [13-18]. Up to now, there are few reports using colloid mesoporous carbon composites to support $MnO_2$ nanomaterials for supercapacitor electrodes to enhance electrochemical performance [22].

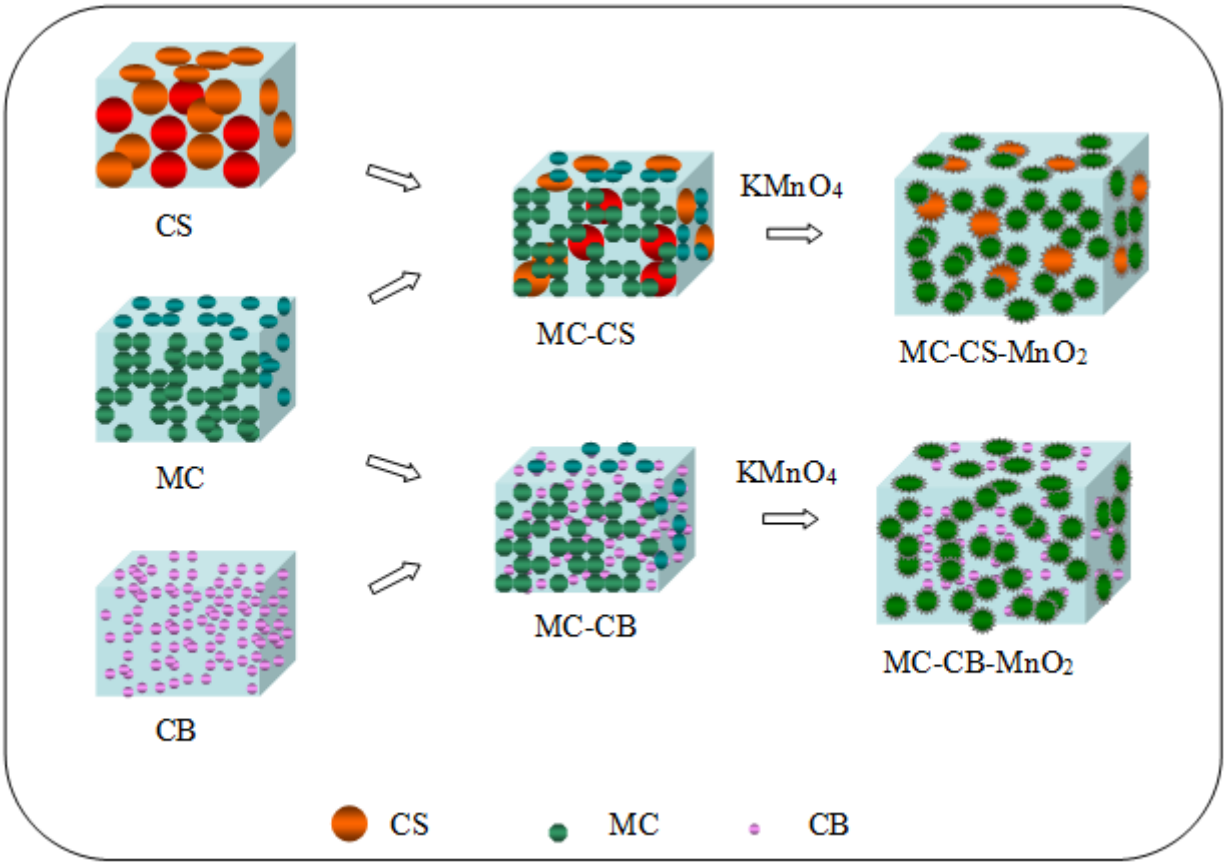


**Figure 1.** Schematic diagram presenting the synthesis process of the as-prepared samples in this work.

In this work, a cost-effective and flexible method has been established to manufacture MC-CS and MC-CB composites, which are utilized as skeletons to support the $MnO_2$. The schematic diagram showing our concept and preparation process is illustrated in Fig. 1. Herein, the three-dimensional (3D) MC-CS-$MnO_2$ and MC-CB-$MnO_2$ nanocomposites are synthesized for the first time, exhibiting higher specific capacitance and stable cycling performance.

## 2. EXPERIMENTAL SECTION

### *2.1 Preparation of MC-CS and MC-CB*

MC-CS and MC-CB was synthesized via a modified hydrothermal method [20,21]. In a typical synthesis, 12 g of glucose and 30 mg of carbon spheres (CS) were dissolved in distilled water (35 mL), followed by the addition of ethylenediamine (EDA) (2 mL). The mixed liquor was poured into a 50-mL autoclave, maintaining at 180 $^{o}$C for 4 h. After being cooled to room temperature, the solid precipitates were gathered by centrifugation, thus obtaining MC-CS after being washed with ethanol and distilled water for several times. Similarly, we used 30 mg of carbon black (CB) instead of carbon spheres and obtained MC-CB.

### *2.1 Synthesis of MC-CS-$MnO_2$ and MC-CB-$MnO_2$*

The MC-CS-$MnO_2$ and MC-CB-$MnO_2$ nanocomposites were prepared by a developed etching method [22]. Typically, MC-CS powders (10 mg) were dispersed into 20 mL of distilled water. After ultrasonication for 10 minutes, $KMnO_4$ solution (5 mL) and $H_2SO_4$ solution (0.8 mL, 50 mM) were added in order. After stirring for 2 h, the mixed liquor was washed, centrifuged and dried at 60 $^{o}$C. The solid precipitates thus obtained are entitled as MC-CS-$MnO_2$-10, MC-CS-$MnO_2$-20, and MC-CS-$MnO_2$-50, representing the different $KMnO_4$ concentrations of 10, 20, and 50 mM, respectively. Furthermore, MC-CB-$MnO_2$-10, MC-CB-$MnO_2$-20, and MC-CB-$MnO_2$-50 were prepared in the same way.

### *2.3. Characterization*

The morphology and structure of as-obtained nanocomposites were characterized by focused ion beam scanning electron microscopy (Zeiss Auriga FIB/SEM). The crystal structures and chemical compositions of as-obtained samples were recorded on powder X-ray diffraction (XRD, D/max 1200, Cu Kα), and thermogravimetric analyzer-differential scanning calorimeter (TGA-DSC NETZSCH STA 449C). The specific surface area was tested by $N_2$ adsorption/desorption isotherm at 77 K, and the pore size distributions were calculated from the adsorption curve by the Barrett-Joyner-Halenda (BJH) method.

### *2.4 Electrochemical measurements*

The electrochemical tests of the as-obtained nanocomposites were conducted using an electrochemical workstation (CHI 660E) in a three-electrode electrochemical cell with the electrolyte of 1 M $Na_2SO_4$ aqueous solution. The saturated calomel electrode (SCE) and platinum plate were used as the reference electrode and the counter electrode, respectively. The working electrode consisted of active materials, carbon black and polyvinylidene difluoride (PVDF) in a mass proportion of 7:2:1,

which was pasted on the nickel foam. To remove the solvent and water, the electrodes were then dried at 120 $^{o}$C under vacuum overnight.

Cycle voltammetry (CV) measurements were enforced in the voltage between 0 and 1.0 V. Galvanostatic charge-discharge tests were carried out at varied current densities in the same potential range as the CV experiments. EIS measurements were performed in a frequency range from 0.01 Hz to 100 kHz at open circuit voltage, applying an AC voltage with 5 mV amplitude. The charge-discharge cycling was performed by 1000 cycles at the current density of 2 A $g^{-1}$.

## 3. RESULTS AND DISCUSSION

XRD patterns of MC-CS-$MnO_2$-20 and MC-CB-$MnO_2$-20 are displayed in Fig. 2, which clearly shows broad peaks at 2θ=37.0$^{o}$ and 65.8$^{o}$, assigning to the (400) and (002) crystal planes of $MnO_2$ (JCPDS no. 44-0141) [23]. It also can be seen that the mesoporous carbon displays an expanding peak around 25 $^{o}$, indicating its amorphous nature. [20].

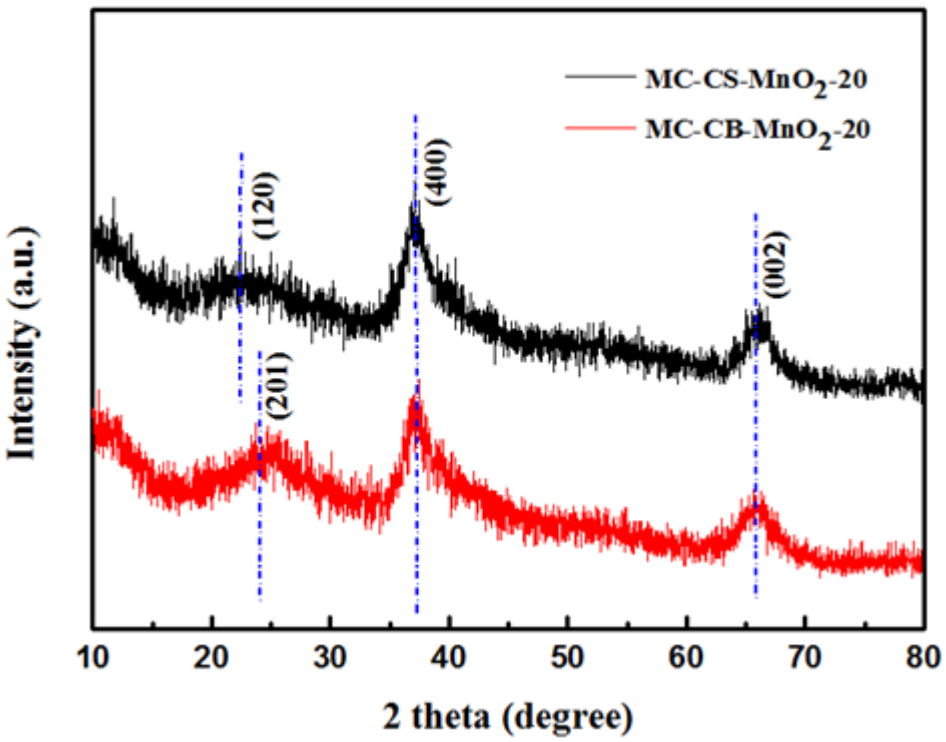


**Figure 2.** XRD patterns of MC-CS-$MnO_2$-20 (a), MC-CB-$MnO_2$-20 (b).

Universally, thermal analysis is employed to estimate the water of crystallization, the content of each component, and to determine decomposition temperature [19], and the TGA results are shown in Fig. 3.

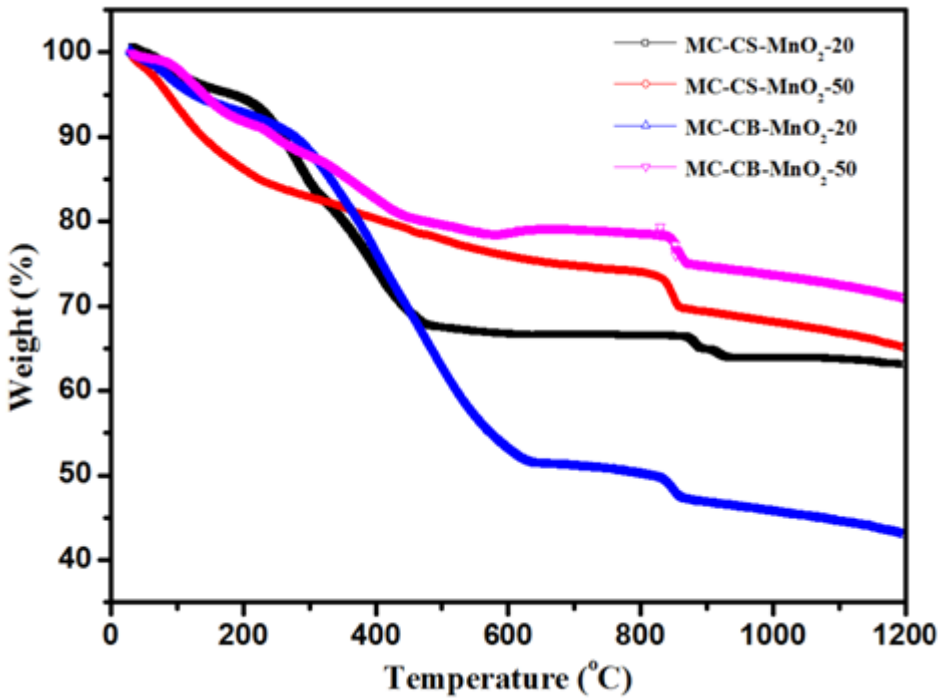


**Figure 3.** TGA curves of MC-CS-$MnO_2$-20, MC-CS-$MnO_2$-50, MC-CB-$MnO_2$-20 and MC-CB-$MnO_2$-50.

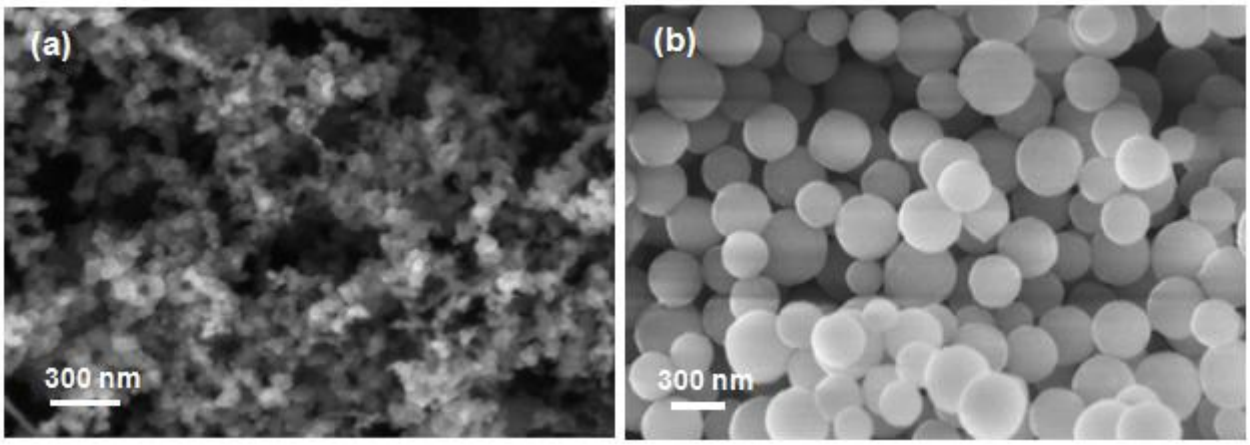


**Figure 4.** Typical SEM images of the CB (a) and CS (b).

For a typical MC-CS-$MnO_2$-20 sample, 6% weight loss below 210 $^oC$ belongs to the removal of physically adsorbed water in the sample [19,30], 27% weight loss from 210 $^oC$ to 470 $^oC$ should be oxidized MC in air, and 4% weight loss from 210 $^oC$ to 470 $^oC$ should belong to the removal of CS. Thus the dry MC-CS-$MnO_2$-20 nanocomposite can be quantified as 0.71$MnO_2$/0.29MC, while MC-CS-$MnO_2$-50, MC-CB-$MnO_2$-20 and MC-CB-$MnO_2$-50 are 0.75$MnO_2$/0.25MC, 0.50$MnO_2$/0.50MC and 0.75$MnO_2$/0.25MC, respectively. These findings suggest that the content of $MnO_2$ could be controlled by using different concentrations of $KMnO_4$ solution.

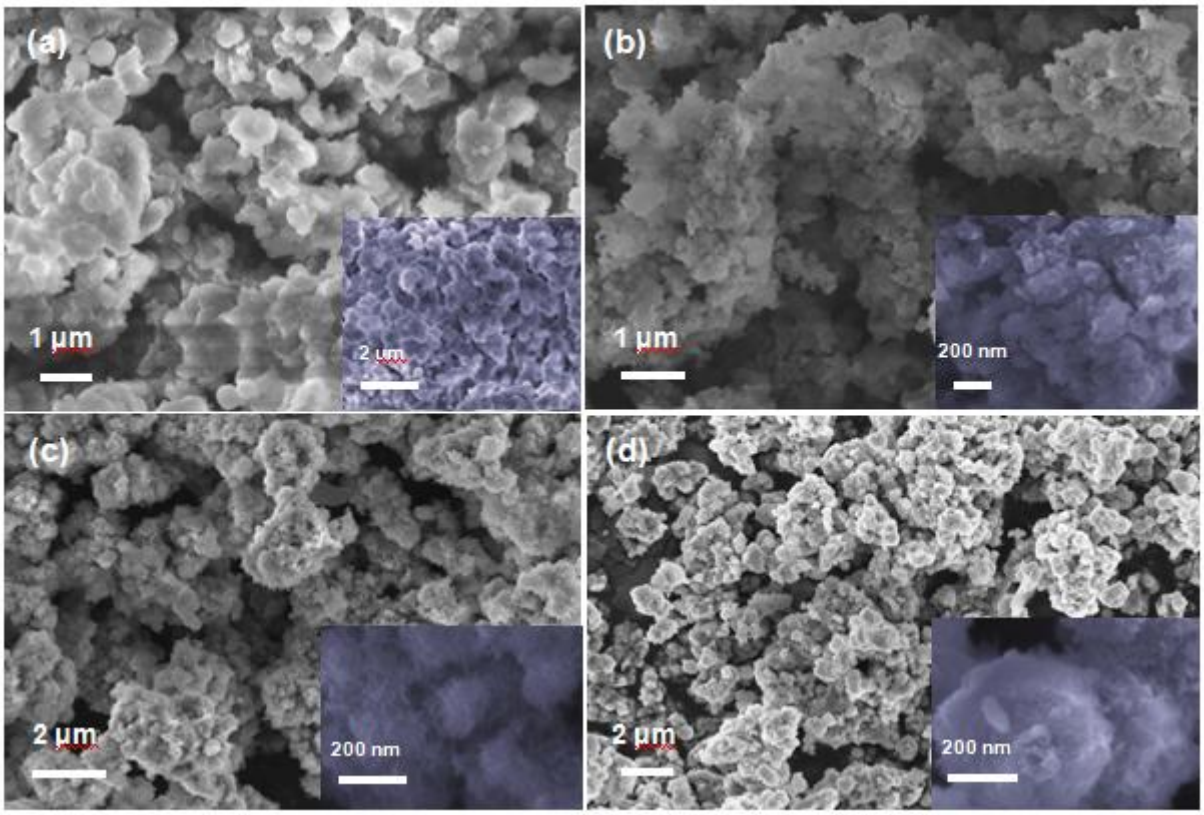


**Figure 5.** SEM images of MC-CS (a), MC-CS-$MnO_2$-10 (b), MC-CS-$MnO_2$-20 (c), and MC-CS-$MnO_2$-50 (d).

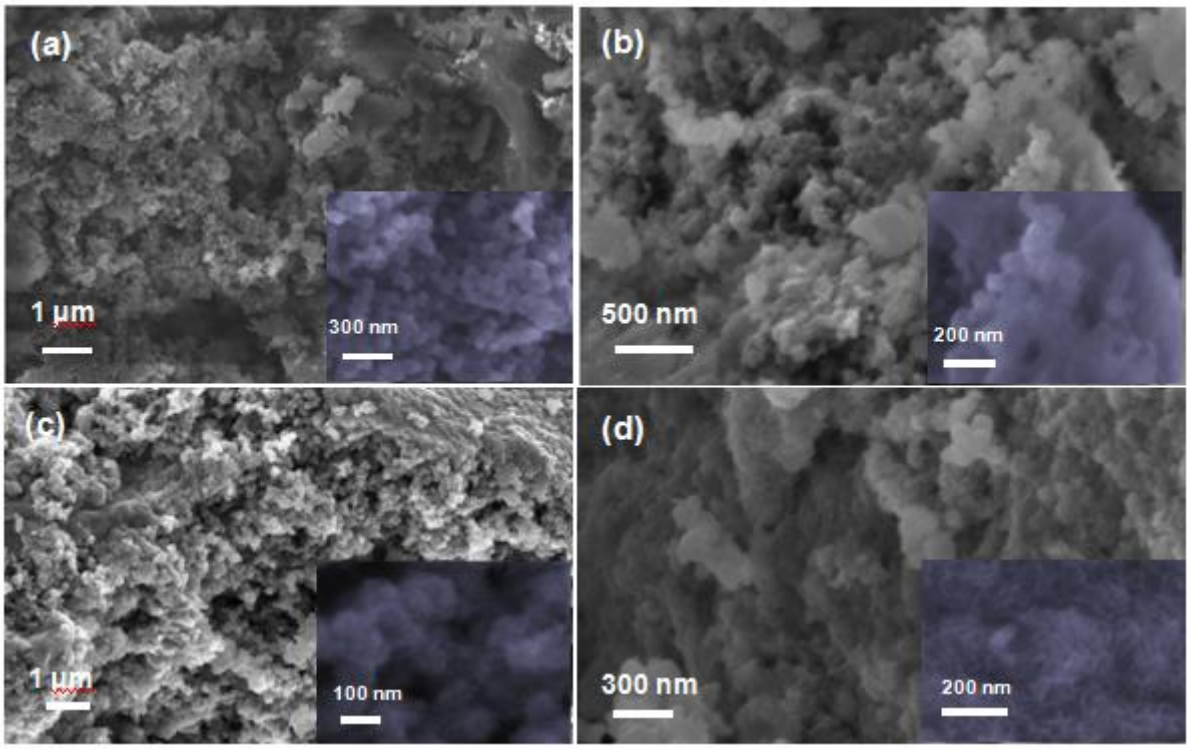


**Figure 6.** SEM images of MC-CB (a), MC-CB-$MnO_2$-10 (b), MC-CB-$MnO_2$-20 (c), and MC-CB-$MnO_2$-50 (d).

The typical SEM images are depicted in Fig. 5 and Fig. 6, clearly showing morphologies and structures of the as-obtained samples.

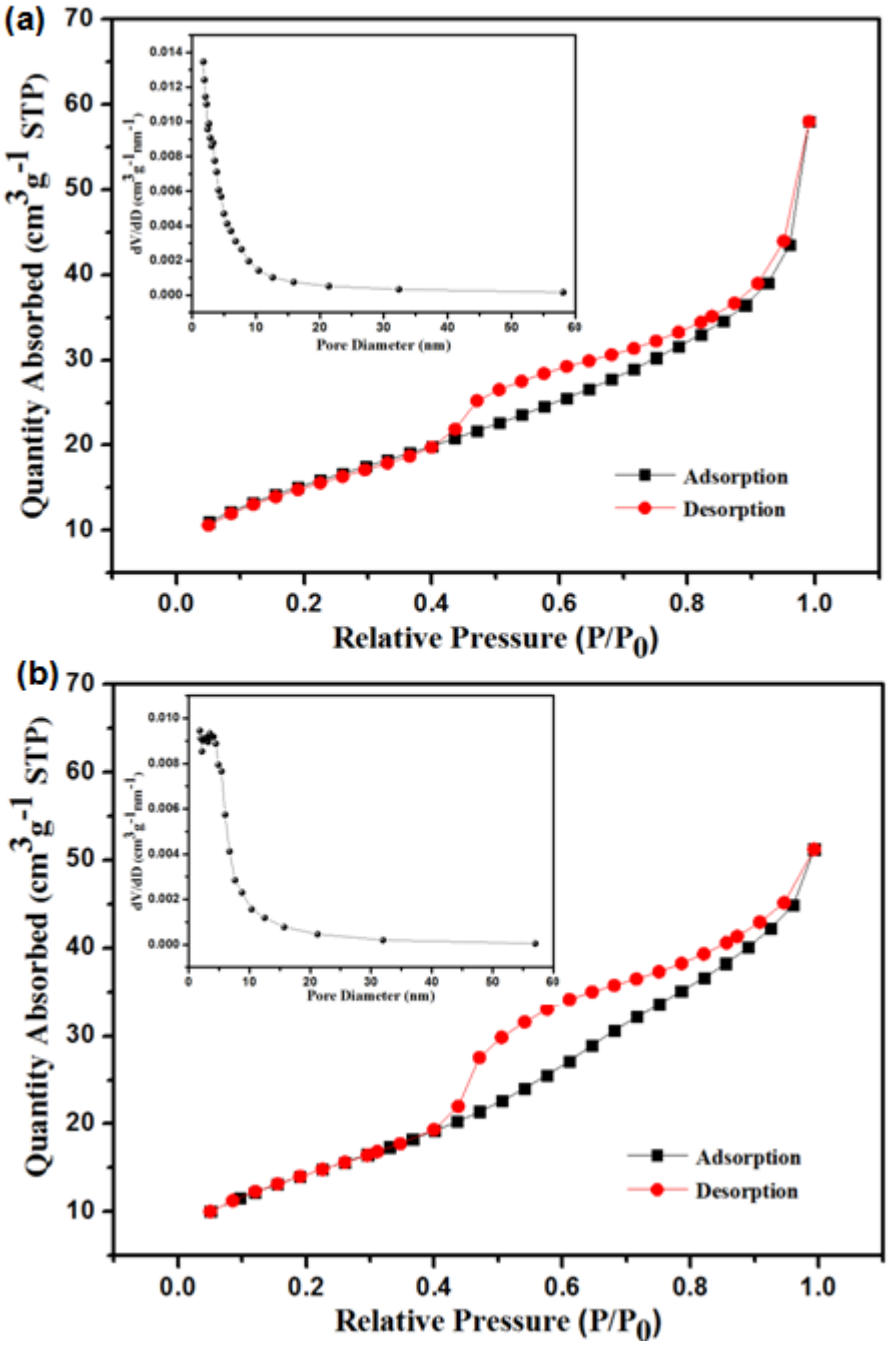


**Figure 7.** $N_2$ adsorption and desorption isotherms and their corresponding pore-size distribution curves (insets) of MC-CS-$MnO_2$-20 (a), MC-CB-$MnO_2$-20 (b).

As displayed in Fig. 5a and Fig. 6a, the MC-CS and MC-CB display a mesoporous nature of pure MC with a continuous skeleton having many pores connected by many nanorods, with CS and CB whose SEM images are illustrated in Fig. 4 doped respectively. As clearly shown in Fig. 5b, c and d, MC-CS-$MnO_2$-10, MC-CS-$MnO_2$-20 and MC-CS-$MnO_2$-50 are uniformly decorated with $MnO_2$ nanosheets, becoming thicker and denser apparently. What's more, the interconnected skeletons which create adequate space ensure more superficial electroactive species and much easier electrolyte ion

transport. Notably, the structure of MC-CS-$MnO_2$ presents a more loose nature with the increasing of the concentration of $KMnO_4$ solution, which might be due to the etching as the skeletons of MC-CS start to collapse. As presented in Fig. 6a, b and c, MC-CB-$MnO_2$-10, MC-CB-$MnO_2$-20 and MC-CB-$MnO_2$-50 look like dense honeycombs made of varying amounts of interconnected particles which form the mesoporous nature. Compared with MC-CS-$MnO_2$-20 and MC-CB-$MnO_2$-20, MC-CS-$MnO_2$-50 and MC-CB-$MnO_2$-50 possess a higher content of $MnO_2$ but an unevener pore structures. All above findings demonstrate that the morphology and pore structure of MC-CS-$MnO_2$ and MC-CB-$MnO_2$ nanocomposites could be controlled by changing the amount of $KMnO_4$. No wonder all of them possess a high specific surface area, owing to their nature of multiholes.

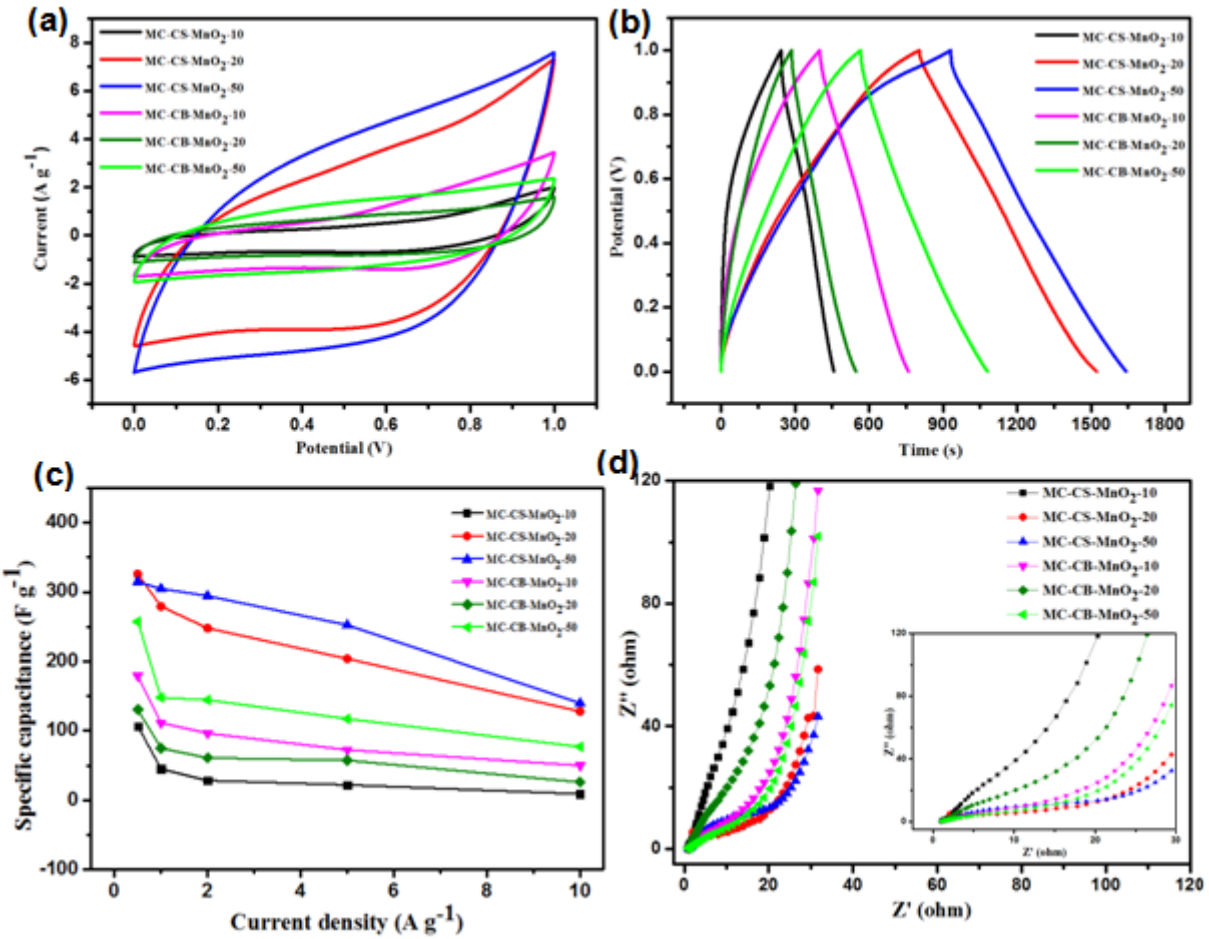


**Figure 8.** The electrochemical performance of the MC-CS-$MnO_2$ and MC-CB-$MnO_2$ nanomaterials electrodes measured in 1 M $Na_2SO_4$ solution. (a) CV curves measured at the scan rate of 50 mV $s^{-1}$. (b) Galvanostatic charge-discharge curves at the current density of 0.5 A $g^{-1}$. (c) Specific capacitance at various current densities. (d) Electrochemical impedance spectrum in the frequency range from 0.01 Hz to 100 kHz at the open potential.

To further understand the surface properties of those nanocomposites, the $N_2$ adsorption-desorption isotherms and the Barrett-Joyner-Halenda (BJH) pore size distribution curves (insets) of MC-CS-$MnO_2$-20 and MC-CB-$MnO_2$-20 are presented in Fig. 7. We can see that all the isotherms of the samples pertain to type IV on the basis of IUPAC classification [24,25], indicating the presence of

mesopores derived from the self-assembly of 2D nanosheet building blocks [26]. From the test we study that MC-CS-$MnO_2$-20 shows the higher specific area of 55.6 $m^2$ $g^{-1}$ compared to that of MC-CB-$MnO_2$-20 (52.6 $m^2$ $g^{-1}$). The BJH pore size distributions derived from the adsorption data suggest that MC-CS-$MnO_2$-20 whose average pore diameter is 6.44 nm approximately possesses a relatively wide pore size distribution. It is generally accepted that the porous characteristics and the large BET surface area of these nanostructures could offer the chance of efficient electrons and ions transport, contributing to the good electrochemical behavior of the materials [20].

The electrochemical properties of MC-CS-$MnO_2$ and MC-CB-$MnO_2$ nanocomposites with different $MnO_2$ content were appraised by CV curves, galvanostatic charge-discharge curves and EIS measurements. Fig. 8a depicts the CV curves at the scan rate of 50 mV $s^{-1}$, exhibiting typical pseudocapacitive behavior without obvious redox peak in the chosen voltage range. Obviously, MC-CS-$MnO_2$-50 demonstrates excellent capacitive and reversible behavior in the voltage between 0 and 1.0 V, which may be originated from the most consumption of the mesoporous carbon [27]. Galvanostatic charge-discharge curves at varied current densities are recorded in Fig. 8b, the curves demonstrate a nearly symmetrical shape with linear slopes reflecting good electrochemical performance and reversibility of the samples.

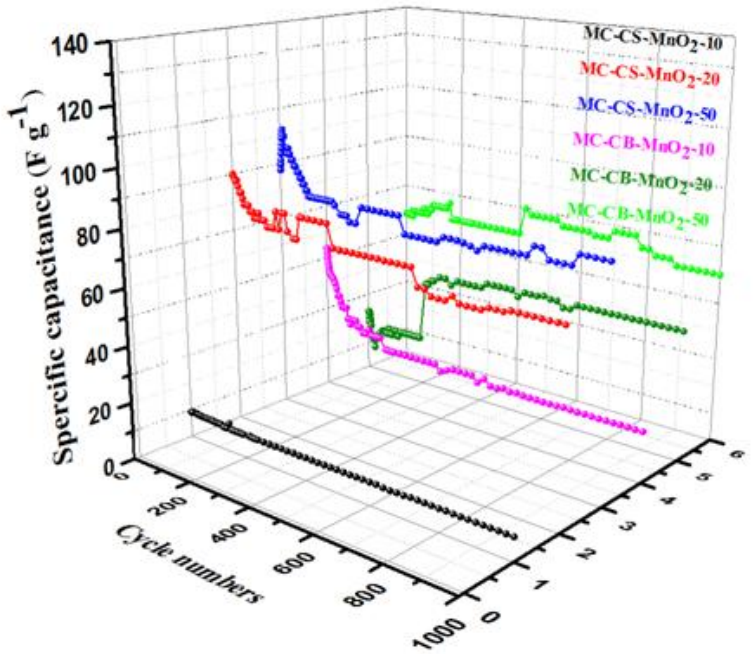


**Figure 9.** Variation of capacitance with cycle number at the current density of 2.0 A $g^{-1}$.

The specific capacitances of MC-CS-$MnO_2$-20, MC-CS-$MnO_2$-50, MC-CB-$MnO_2$-20 and MC-CB-$MnO_2$-50 are calculated to be 326, 315, 130.75 and 257.5 F $g^{-1}$ at the current density of 0.5 A $g^{-1}$, respectively according to Eq. (1) [26,28,29]. Note that, MC-CS-$MnO_2$ shows a more potential capacitance than that of MC-CB-$MnO_2$ and MC-$MnO_2$-50 (270.5 F $g^{-1}$) [20]. There is no doubt that this owes to the novel structure of MC-CS with interconnected skeleton and reasonable pore structure.

As it can be seen in Fig. 8c, capacitance values decrease when the current density increases. Despite all this, the samples still reveal relatively better rate capability.

EIS experiments of these as-obtained samples were carried out in the frequency from 0.01 to 100 kHz, as shown in Fig. 8d. Detailedly, the Nyquist plots of the six profiles are similar in shape, consisted of a linear component in the low frequency region and partial semicircle at high frequency. The impedance spectra can be fitted by using Zsimpwin according to the equivalent circuit [22,26]. From the inset in Fig. 8d, the interfacial Faradic charge tranfer resistance $R_{ct}$ values of MC-CS-$MnO_2$-10, MC-CS-$MnO_2$-20, MC-CS-$MnO_2$-50, MC-CB-$MnO_2$-10, MC-CB-$MnO_2$-20 and MC-CB-$MnO_2$-50 are estimated to be about 6.65, 3.45, 5.1, 4.35, 4.5 and 4.25 Ù, and ohmic resistance of the electrolyte and the internal resistance of the active material $R_s$ values are about 1.46, 1.21, 0.73, 1.13, 2.85,1.77 and 1.06 Ù, respectively.

Electrochemical stability is an important factor on the performance of supercapacitor devices. It is worth noting that supercapacitors ought to run safely and steadily, requiring the specific capacitance to change as little as possible. Thus the cycle stability was further investigated by repeating the CV measurements at the current density of 2 A $g^{-1}$ for 1000 cycles, as depicted in Fig. 9. After 1000 cycles, 88.89%, 73.66%, 91.33%, 33.46%, 200% and 102.74% of the pristine capacitance is retained for MC-CS-$MnO_2$-10, MC-CS-$MnO_2$-20, MC-CS-$MnO_2$-50, MC-CB-$MnO_2$-10, MC-CB-$MnO_2$-20 and MC-CB-$MnO_2$-50, respectively, signifying good electrochemical stability as the supercapacitor electrode material. What is the most surprising is that an augment of 100% on specific capacitance for MC-CB-$MnO_2$-20 is found after 1000 cycles, which is ascribed to the activation effect of electrochemical cycling [20].

## 4. CONCLUSIONS

In conclusion, the three-dimensional (3D) nanocomposites of diverse carbon materials, (e.g., mesoporous carbon (MC) filled with carbon spheres (CS) and carbon blacks (CB)) and $MnO_2$ were synthesized for the first time. Among all the samples MC-CS-$MnO_2$-20 and MC-CS-$MnO_2$-50 demonstrated the larger specific capacitance of 326 F $g^{-1}$ and 315 F $g^{-1}$, while MC-CB-$MnO_2$-20 and MC-CB-$MnO_2$-50 presented excellent cycling stability, demonstrating an augment on specific capacitance after 1000 cycles. Furthermore, the as-obtained nanocomposites revealed excellent pseudocapacitance performance attributing to the distinct structure of MC-CS and MC-CB, signifying great prospects to be active material for flexible, cost-effective and environment friendly supercapacitors.

ACKNOWLEDGEMENTS
The authors gratefully acknowledge the financial supports provided by National Natural Science Foundation of China (Grant no. 61474011), and Laboratory of Precision Manufacturing Technology, CAEP (KF13004).

## References

1. Z. G. Zhu, Y. J. Hu, H. Jiang, C. Z. Li, *J. Power Sources*, 246 (2014) 402.
2. D. Zhou, H. M. Lin, F. Zhang, H. Niu, L. R. Cui, Q. Wang, F. Y. Qu, *Electrochim. Acta*, 161

(2015) 427.
3. X. M. Ma, L. H. Gan, M. X. Liu, P. K. Tripathi, Y. H. Zhao, Z. J. Xu, D. Z. Zhu, L. W. Chen, *J. Mater. Chem. A.*, 2 (2014) 8407.
4. D. Z. Zhu, Y. W. Wang, L. H. Gan, M. X. Liu, K. Cheng, Y. H. Zhao, X. X. Deng, D. M. Sun, *Electrochim. Acta*, 158 (2015) 166 .
5. Y. T. Hu, H. J. Liu, Q. Q. Ke, J. Wang, *J. Mater. Chem. A*, 2 (2014) 11753.
6. L. M. Liao, C. X. Pan, *Soft Nanosci. Lett.*, 1 (2011).
7. Y. L. Chen, L. H. Du, P. H. Yang, P. Sun, X. Yu, W. J. Mei, *J. Power Sources*, 287 (2015) 68.
8. J. Zhang, J. Ma, J. Jiang, X.S. Zhao, *J. Mater. Res.*, 25 (2011) 1476.
9. Y. X. Zhang, S. J. Zhu, M. Dong, C. P. Liu, Z. Q. Wen, *Int. J. Electrochem. Sci.*, 8 (2013) 2407.
10. L. Qiang, J. H. Liu, J. H. Zou, A. Chunder, Y. Q. Chen, Z. Lei, *J. Power Sources*, 196 (2011), 565.
11. Y. Hou, Y. W. Cheng, T. Hobson, J. Liu, *Nano Lett.*, 10 (2010) 2727.
12. W. J. Wang, Q. L. Hao, W. Lei, X. F. Xia, X. Wang, *J. Power Sources*, 269 (2014), 250.
13. S. K. Kim, E. Jung, M. D. Goodman, K. S. Schweizer, N. Tatsuda, K. Yano, P. V. Braun, *ACS Appl. Mater. Interfaces*, 7 (2015).
14. M. Kaempgen, C. K. Chan, J. Ma, Y. Cui, G. P. Gruner, *Nano Lett.*, 9 (2009) 1872.
15. J. J. Yoo, K. Balakrishnan, J. Huang, V. Meunier, B. G. Sumpter, A. Srivastava, M. Conway, A. L. Mohana Reddy, J. Yu, R. Vajtai, P. M. Ajayan, *Nano Lett.*, 11 (2011) 1423.
16. S. Chen, J. W. Zhu, X. D. Wu, Q. F. Han, X. Wang, *Acs Nano*, 4 (2010) 2822.
17. Y. L. Wang, B. B. Chang, D. X. Guan, X. P. Dong, *J. Solid State Electrochem.*, 19 (2015) 1783.
18. C. W. Huang, C. H. Hsu, P. L. Kuo, C. T. Hsieh, H. Teng, *Carbon*, 49 (2011) 895.
19. J. J. Ma, S. J. Zhu, Q. Y. Shan, S. F. Liu, Y. X. Zhang, F. Dong, H. D. Liu, *Electrochim. Acta*, 168 (2015) 97.
20. Y. X. Zhang, S. J. Zhu, X. D. Hao, C. P. Liu, Z. Q. Wen, *Ceram. Int.*, 40 (2014) 13381.
21. Z. Y. Liu, C. L. Zhang, L. Luo, Z. Chang, X. M. Sun, *J. Mater. Chem.*, 22 (2012) 12149.
22. Y. X. Zhang, M. Dong, S. J. Zhu, C. P. Liu, Z. Q. Wen, *Mater. Res. Bull*, 49 (2014) 448.
23. C. J. Xu, B. H. Li, H. D. Du, F. Y. Kang, Y. Q. Zeng, *J. Power Sources*, 184 (2008) 691.
24. M. Kruk, M. Jaroniec, *Chem. Mater.*, 13 (2001) 3169.
25. G. Y. Gor, M. Thommes, K. A. Cychosz, A. V. Neimark, *Carbon*, 50 (2012) 1583.
26. F. Li, Y. Xing, M. Huang, K. L. Li, T. T. Yu, Y. X. Zhang, D. Losic, *J. Mater. Chem. A.*, 3 (2015).
27. W. Wei, X. Huang, Y. Tao, K. Chen, X. Tang, *Phys. Chem. Chem. Phys.*, 14 (2012) 5966.
28. Y. X. Zhang, M. Kuang, M. Huang, Z. Q. Wen, *Int. J. Electrochem. Sci.*, 8 (2013) 9723.
29. Y. X. Zhang, F. Li, M. Huang, *Mater. Lett.*, 112 (2013) 203.
30. S. H. Li, L. Qi, L. H. Lu, H. Y. Wang, *J. Solid State Chem.*, 197 (2013) 29.